PHYSICAL REVIEW B **89**, 155109 (2014)

Mechanism of structural phase transitions in $KCrF_3$

Carmine Autieri
Dipartimento di Fisica "E.R. Caianiello," Università di Salerno, I-84084 Fisciano (SA), Italy
and Institute for Advanced Simulation, Forschungszentrum Jülich, 52425 Jülich, Germany

Erik Koch
German Research School for Simulation Sciences, 52425 Jülich, Germany
and JARA High-Performance Computing, RWTH Aachen University, 52062 Aachen, Germany

Eva Pavarini
Institute for Advanced Simulation, Forschungszentrum Jülich, 52425 Jülich, Germany
and JARA High-Performance Computing, RWTH Aachen University, 52062 Aachen, Germany

(Received 19 December 2013; revised manuscript received 25 March 2014; published 8 April 2014)

We study the origin of the cubic to tetragonal and tetragonal to monoclinic structural transitions in $KCrF_3$, and the associated change in orbital order, paying particular attention to the relevance of super-exchange in both phases. We show that super-exchange is not the main mechanism driving these transitions. Specifically, it is not strong enough to be responsible for the high-temperature cubic to tetragonal transition and does not yield the type of orbital order observed in the monoclinic phase. The energy difference between the tetragonal and the monoclinic structure is tiny, and most likely results from the interplay between volume, covalency, and localization effects. The transition is rather driven by Slater exchange than super-exchange. Nevertheless, once the monoclinic distortions are present, super-exchange helps in stabilizing the low-symmetry structure. The orbital order we obtain for this monoclinic phase is consistent with the magnetic transition at 80 K.

DOI: 10.1103/PhysRevB.89.155109 PACS number(s): 75.25.Dk, 75.30.Et, 71.70.Ej

I. INTRODUCTION

The Mott insulator $KCrF_3$ (high-spin $t_{2g}^3 e_g^1$ electronic configuration) is isoelectronic to $LaMnO_3$, the mother compound of colossal magnetoresistance materials, but differently from $LaMnO_3$ it exhibits a series of structural and magnetic phase transitions [1,2]. At temperatures higher than 973 K it is a cubic perovskite, between 973 and 250 K it is tetragonal, and finally below 250 K it becomes monoclinic. The tetragonal and monoclinic structures are shown in Fig. 1. At the 973-K transition, with the lowering of the symmetry from cubic to tetragonal a cooperative Jahn-Teller (JT) distortion develops [1]. It is of G type (short and long CrF bonds alternate in all directions), while in $LaMnO_3$ the order is instead of C type (short and long bonds alternate in the **ab** plane and repeat along the **c** direction). Thus below 973 K the system is orbitally ordered. Finally, $KCrF_3$ becomes magnetic below $T_{\mathrm{N}} \sim 80$ K; the ordering vector is $(1/2 \pm \delta, 1/2 \pm \delta, 0)$, corresponding to an antiferromagnetic A-type order with an incommensurate component δ which disappears at 46 K [2]. The phase transitions of $KCrF_3$ have been intensively investigated [1–5], but their nature, and in particular the role played by the purely electronic super-exchange mechanism in the structural transitions, is to date not fully understood.

In recent years we have studied the origin of G- and C-type Jahn-Teller distortions in $KCuF_3$, $LaMnO_3$, and rare-earth manganites [6–8]. We have shown that, although Kugel-Khomskii (KK) many-body super-exchange [9] is very large, it appears to have little influence on the high-temperature orbital-order to orbital-disorder transition observed experimentally [10] in the full series of rare-earth manganites. However, in particular in $LaMnO_3$, super-exchange effects turned out to be so strong that, if hypothetically the static Jahn-Teller distortion was absent, it could alone explain an orbital-order transition at temperatures as large as 500 K. Remarkably, $KCrF_3$ exhibits a change in the co-operative Jahn-Teller distortion around 250 K; in the monoclinic phase the orbital-order acquires a small C-type component in the yz plane, where the pseudocubic **z** and **y** axes are defined as $(\mathbf{a}+\mathbf{b})/2$ and $(\mathbf{a}-\mathbf{b})/2$ (see Fig. 1). Thus, super-exchange could play an important role for the tetragonal to monoclinic structural phase transition, or in similar low-temperature phase transitions observed in other systems. In this work we want to clarify if that is the case.

The paper is organized as follows. In Sec. II we discuss the methods and models used. In Sec. III we present our results. In Sec. III A we discuss the electronic structure, obtained using density-functional theory (DFT) in the generalized-gradient approximation [11] (GGA). In Sec. III B we focus on the super-exchange mechanism for orbital order; by using the density-functional theory + dynamical mean-field theory (DFT+DMFT) method [12,13], we calculate for each structure the transition temperature, as well as the occupied orbitals using the technique introduced in Ref. [6]. We study both the cubic to tetragonal and tetragonal to monoclinic structural phase transitions. In Sec. III C we investigate the effect of the changes in volume by using density-functional theory in the GGA as well as the GGA + U approach [14–16]. In Sec. III D we discuss the origin of the magnetic structure in the monoclinic phase. Finally, Sec. IV gives our conclusions.

II. MODEL AND METHOD

We calculate the electronic structure in the different phases and optimize the structures *ab-initio* using the projected

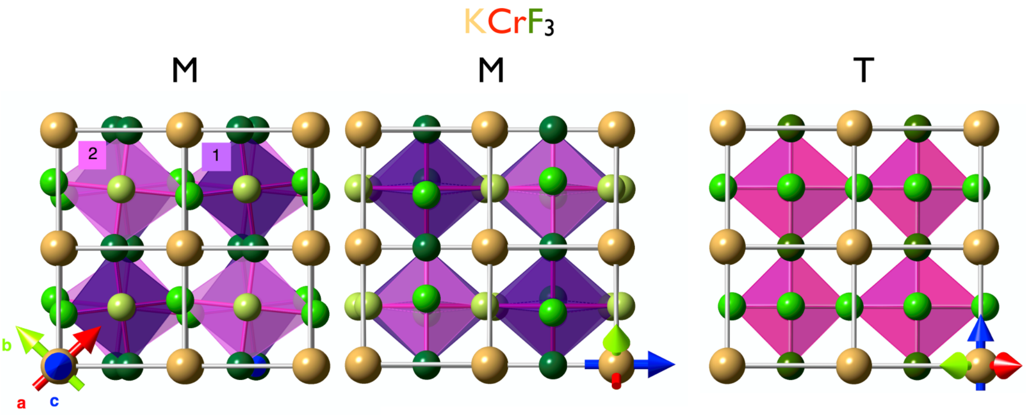

FIG. 1. (Color online) The monoclinic (M, left and center) and tetragonal structure (T, right) of $KCrF_3$. Atoms: K (large spheres), F [intermediate size spheres; different shades (light/dark) show inequivalent F atoms] forming octahedra around Cr centers. For the monoclinic structure the figure on the left shows the tilting of the octahedra about the $\mathbf{c}$ axis; the octahedra do not rotate, as shown by the central figure. To better illustrate these distortions, two consecutive planes in direction $\mathbf{c}$ (left figure) or $\mathbf{a}-\mathbf{b}$ (center figure) are shown. With respect to the tetragonal structure, long and short Cr-F bonds shrink at sites labeled as type 1 and elongate at sites labeled as type 2. The pseudocubic directions are defined as follows. Tetragonal structure: $\mathbf{x} \sim (\mathbf{a}+\mathbf{b})/2$, $\mathbf{y} \sim (-\mathbf{a}+\mathbf{b})/2$, and $\mathbf{z} \sim \mathbf{c}/2$. For the $i=1$ site the long (short) bond is along $\mathbf{x}$ ($\mathbf{y}$) direction. Monoclinic structure: $\mathbf{x} \sim \mathbf{c}/2$, $\mathbf{y} \sim (\mathbf{a}-\mathbf{b})/2$ and $\mathbf{z} \sim (\mathbf{a}+\mathbf{b})/2$. For the octahedron $i=1$ site the long (short) bond is along $\mathbf{x}$ ($\mathbf{y}$) direction. This choice of pseudocubic axes allows direct comparison between the structure in the two phases: The figure on the left for the monoclinic and figure on the right for the tetragonal show the same view (yz plane, site of type 1 on the right top corner).

augmented plane-wave technique as implemented in the ABINIT code [17,18] and in the VASP package [19]. We construct Wannier functions via the Marzari-Vanderbilt localization procedure (Wannier90 code [20]) as well as via the first-principles downfolding approach based on the Nth-order muffin-tin orbital (NMTO) method [21], obtaining similar results.

To study the effects of the Kugel-Khomskii super-exchange mechanism we use *ab-initio* minimal many-body models. The Cr d bands split into half filled t_{2g} and $1/4$ filled e_g bands; the system is in the high-spin $t_{2g}^3 e_g^1$ configuration. The Hund's rule interaction between t_{2g} and e_g electrons yields a magnetic coupling of the e_g electrons to the effective spin of t_{2g} electrons, $\mathbf{S}_{t_{2g}}$. The latter acts as an effective magnetic field $h = JS_{t_{2g}}$ and, in the paramagnetic phase, yields a band-renormalization factor accounting for t_{2g} spin disorder [22]. Thus the minimal model is the two-band Hubbard model

$$\begin{aligned} H = & \sum_{im\sigma}\sum_{i'm'\sigma'} t^{i,i'}_{m,m'} u^{i,i'}_{\sigma,\sigma'} c^\dagger_{im\sigma} c_{i'm'\sigma'} \\ & - h\sum_{im}(n_{im\Uparrow} - n_{im\Downarrow}) + U\sum_{im} n_{im\Uparrow} n_{im\Downarrow} \\ & + \frac{1}{2}\sum_{im(\neq m')\sigma\sigma'} (U - 2J - J\delta_{\sigma,\sigma'}) n_{im\sigma} n_{im'\sigma'}. \qquad (1) \end{aligned}$$

In this model $c^\dagger_{im\sigma}$ creates an electron with spin $\sigma = \Uparrow,\Downarrow$ in a Wannier orbital $|m\rangle = |x^2-y^2\rangle$ or $|3z^2-r^2\rangle$ at site i, and $n_{im\sigma} = c^\dagger_{im\sigma} c_{im\sigma}$. $\Uparrow$ ($\Downarrow$) indicates the e_g spin parallel (antiparallel) to the t_{2g} spins on the same site. The matrix u accounts for the orientational disorder of the t_{2g} spins, $u^{i,i'}_{\sigma,\sigma'} = 2/3$ for $i \neq i'$, $u^{i,i}_{\sigma,\sigma'} = \delta_{\sigma,\sigma'}$. The parameter $t^{i,i'}_{m,m'}$ is the hopping integral from orbital m on site i to orbital m' on site i'. The on-site terms $t_{m,m'} = \varepsilon_{m,m'}$ give the crystal-field splitting. U and J are the direct and exchange terms of the screened on-site Coulomb interaction. The Wannier basis provides us with *ab-initio* values of the hopping integrals and crystal-field splittings. We calculate the average Coulomb interaction [13,23] $U_{\rm av} - J_{\rm av}$ using the linear-response approach [24]. We find that $U_{\rm av} - J_{\rm av}$ varies from $\sim$3 eV in the tetragonal phases to $\sim$4 eV in the monoclinic phase. The same approach yields $U_{\rm av} - J_{\rm av} \sim 2.7$ eV for $LaMnO_3$. The theoretical estimate for $J_{\rm av}$ is $\sim$0.75 eV [25]. This approach leads to $U \sim U_{\rm av} + 8/7 J_{\rm av} \sim$ 5–6 eV. The GGA band structure in the different phases is shown in Fig. 2.

We solve the two-band Hubbard model (1) by means of the DFT+DMFT technique [12,13]. We use as impurity solver both the Hirsch-Fye (HF) [26] quantum Monte Carlo (HF-QMC) technique as well as the hybridization-expansion continuous-time QMC approach (CT-QMC) [27] in the implementation presented in Ref. [28]. To allow for orbital order, we use a full self-energy matrix in spin-orbital space, and when necessary, we allow for inequivalent sites using the cellular cluster DMFT approach. We have recently shown [28] that in e_g systems such as (1) spin-flip and pair-hopping terms do not affect the super-exchange orbital-ordering transition temperature $T_{\rm KK}$, and therefore we neglect them to speed up calculations. We have also shown that the exact value of h does not affect the strength of super-exchange [7] as far as h is large enough to yield the correct Hund's rule multiplet structure. Thus we use the theoretical estimate for $LaMnO_3$ $h = 2JS_{t_{2g}} \sim 2.7$ eV [29]. Our DFT+DMFT code is optimized to exploit the power of modern massively parallel architectures; details on the performance of our code for $N_o = 1$ to $N_o = 5$, where N_o is the number of orbitals, and both the HF-QMC and the hybridization-expansion CT-QMC solver can be found in Ref. [28].

In order to study the effects of volume expansion, covalency, and localization we use the full Hamiltonian and the GGA + U and SGGA + U approach, where SGGA stands for spin-polarized GGA. The DFT + U approach is less

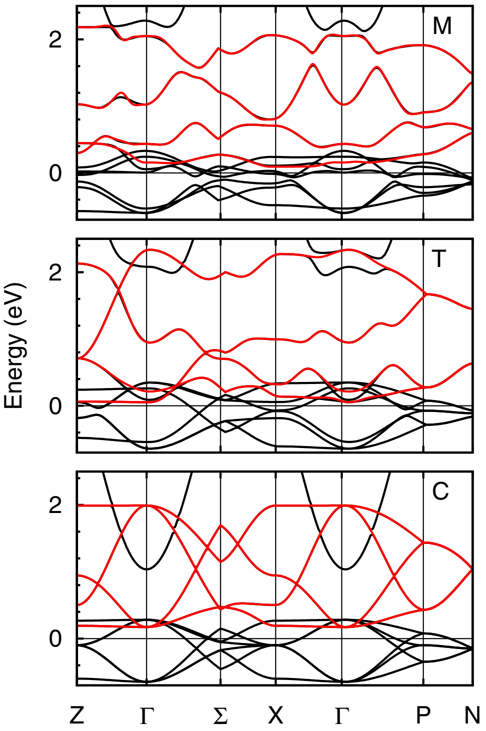

FIG. 2. (Color online) Dark lines: GGA band structure for the cubic (C), tetragonal (T), and monoclinic (M) phase. The Fermi level is set at energy zero. Light lines: e_g-like bands from maximally localized Wannier functions plotted on top of the GGA bands. The remaining bands are the Cr t_{2g} bands, crossing the Fermi level and partially filled, and the empty Cr 4*s* bands.

computationally demanding than DFT + DMFT, but, as will become clear in the next sections, for this specific purpose as suitable as DFT + DMFT. We perform GGA + U calculations for different volumes, U varying from 4 up to 9 eV. Finally, we calculate the magnetic coupling and the magnetic anisotropy by combining many-body perturbation theory (based on *ab-initio* hopping parameters and Coulomb integrals) and direct first-principles SGGA + U calculations.

III. RESULTS

A. Electronic structure

We find that the overall bandwidth of the e_g and t_{2g} bands remains about the same in all the structures, $W_{t_{2g}} \sim 1$ eV, $W_{e_g} \sim 2.3$ eV, perhaps $W_{t_{2g}}$ slightly decreases and W_{e_g} slightly increases reducing the symmetry. The bands themselves are, however, sizably deformed by the distortions, as can be seen in Fig. 2.

We calculate the hopping integrals and crystal-field parameters for the e_g bands by constructing e_g Wannier functions by projection. The most important hopping integrals are listed in Table I. This table shows that the Jahn-Teller crystal-field splitting progressively increases in the series of phase transitions, while the main hopping integral, the hopping along the **z** direction, decreases. Thus, contrary to naive expectations, the hopping integrals do not increase as the volume shrinks, because the lattice distortions increase as well, leading to a reduction of the matrix elements due to Slater-Koster factors. In the monoclinic case two neighboring Cr sites are inequivalent and have different splittings. We define the lowest energy crystal-field state as $|\theta_{\rm CF}\rangle = \cos\frac{\theta_{\rm CF}}{2}|3z^2-r^2\rangle + \sin\frac{\theta_{\rm CF}}{2}|x^2-y^2\rangle$. Our calculations yield $\theta_{\rm CF} = \theta^2_{\rm CF} \sim 111^\circ = -\theta^1_{\rm CF}$ in the tetragonal phase, where $\theta^i_{\rm CF}$ is the angle for site i. In the monoclinic phase we find $\theta^1_{\rm CF} \sim -120^\circ$ and $\theta^2_{\rm CF} \sim 112^\circ$. The sites and the pseudocubic axes are defined in Fig. 1.

B. Kugel-Khomskii super-exchange mechanism

First we analyze the purely electronic Kugel-Khomskii super-exchange mechanism. We calculate $T^{\rm T}_{\rm KK}$, the Kugel-Khomskii critical temperature for the transition from cubic to tetragonal, by using the approach of Ref. [6]. We explain it here in short. Starting from the experimental tetragonal structure we progressively reduce the Jahn-Teller and tetragonal crystal-field splitting to zero and perform single-site DFT+DMFT calculations for the corresponding idealized structures, decreasing the temperature to search for the orbital order phase transition. In the DMFT calculation we use a $N_o \times N_o$ self-energy matrix per spin, where $N_o = 2$ is the number of orbitals;

TABLE I. Nearest neighbor hopping integrals $t^{i,i'}_{m,m'}$ and crystal-field matrix elements $\varepsilon_{m,m'}$ in the e_g-like basis, with $|1\rangle = |x^2-y^2\rangle$ and $|2\rangle = |3z^2-r^2\rangle$. All energies are in meV. For the crystal-field levels we take $\varepsilon_{1,1}$ at site 1 as energy zero. The spin-orbit coupling constants $\lambda_\parallel$ and $\lambda_\perp$, with $H_{\rm SO} = \lambda_\parallel L_z S_z + \frac{1}{2}\lambda_\perp(L_+S_- + L_-S_+)$, are also given. The directions (lmn) are defined $l\mathbf{x} + m\mathbf{y} + n\mathbf{z}$ where **x**, **y** and **z** are the pseudocubic axes defined in Fig. 1.

	Cubic			Tetragonal			Monoclinic			
lmn	$t^{i,i'}_{1,1}$	$t^{i,i'}_{1,2}$	$t^{i,i'}_{2,2}$	$t^{i,i'}_{1,1}$	$t^{i,i'}_{1,2}$	$t^{i,i'}_{2,2}$	$t^{i,i'}_{1,1}$	$t^{i,i'}_{1,2}$	$t^{i,i'}_{2,1}$	$t^{i,i'}_{2,2}$
100	−223	124	−80	−171	157	−95	−164	121	83	−72
010	−223	−124	−80	−171	−109	−95	−163	−87	−167	−67
001	−9	0	−294	47	−73	−292	33	−72	52	−253
	$\varepsilon_{1,1}$	$\varepsilon_{2,2}$	$\varepsilon_{1,2}$	$\varepsilon_{1,1}$	$\varepsilon_{2,2}$	$\varepsilon_{1,2}$		$\varepsilon^{\rm Cr1}_{1,1}$	$\varepsilon^{\rm Cr1}_{2,2}$	$\varepsilon^{\rm Cr1}_{1,2}$
000	0	0	0	0	310	390		0	466	414
								$\varepsilon^{\rm Cr2}_{1,1}$	$\varepsilon^{\rm Cr2}_{2,2}$	$\varepsilon^{\rm Cr2}_{1,2}$
								111	368	−316
$\lambda_\parallel$	7			15			34			
$\lambda_\perp$	2			3			4			

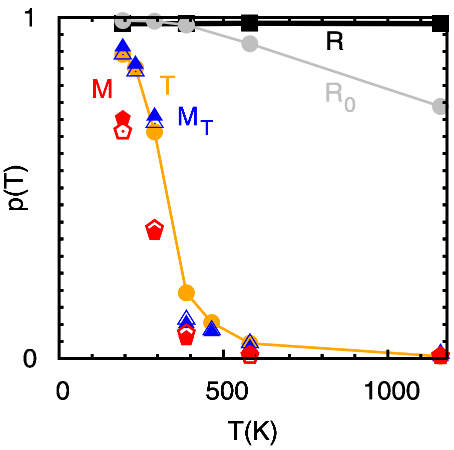

FIG. 3. (Color online) Orbital polarization $p(T)$, defined as the difference in occupation between most occupied and least occupied orbitals for several structures. R: experimental tetragonal structure. R$_0$: idealized tetragonal structure in which the Jahn-Teller distortion has been removed. T: idealized tetragonal structure with no crystal-field splitting. M: idealized monoclinic structure with no crystal-field splitting. For the latter the results are obtained via two-site cellular cluster DMFT calculations in two different ways, (i) from the idealized tetragonal structure T using a supercell with monoclinic symmetry (triangles, labeled M$_T$) and (ii) from the monoclinic structure directly (pentagons, labeled M); the two inequivalent sites are distinguished in the plot via empty and full symbols.

we use point-group symmetry to build the self-energy matrix for different sites. We calculate the orbital polarization $p(T)$, defined as the difference in occupation between the least and most occupied orbital, as a function of the temperature T. The results are shown in Fig. 3 for several cases; the curve obtained with the experimental tetragonal structure (labeled with R in the figure) is flat, $p(T) \sim 1$, hence the system is always orbitally ordered even at temperatures as high as 1500 K. Progressively reducing the distortions we can disentangle the effect of super-exchange from that of a static crystal field. Figure 3 shows the reduction of orbital polarization at high temperature for the case in which the Jahn-Teller splitting is removed, hence the crystal-field splitting is sizably reduced (curve labeled with R_0). In the zero crystal-field limit (T in the figure) the transition is due to super-exchange only and occurs at a temperature $T_{\rm KK}^{\rm T}$. We find that $T_{\rm KK}^{\rm T} \sim 400$ K, a value similar to the result we have previously obtained for KCuF$_3$. When we define the DMFT occupied state as $|\theta\rangle = \cos\frac{\theta}{2}|3z^2 - r^2\rangle + \sin\frac{\theta}{2}|x^2 - y^2\rangle$, we find $\theta = -\theta_1 = \theta_2 \sim 90^\circ$, where θ_i is the angle for a site of type i (see Fig. 1). The transition temperature $T_{\rm KK}^{\rm T}$ is too small for super-exchange being responsible for the high-temperature cubic to tetragonal cooperative Jahn-Teller distortion above 900 K. Furthermore, the tetragonal crystal field works against super-exchange [7,28], leading to an occupied state with $\theta \sim 180^\circ$ once the tetragonal lattice distortions are taken into account. This is in line with the results for KCuF$_3$ and REMnO$_3$ systems [6–8]. Nevertheless, $T_{\rm KK}^{\rm T}$ is sizably higher than the tetragonal to orthorhombic transition temperature, 250 K, and thus well below $T_{\rm KK}^{\rm T}$ super-exchange could win and even rotate the angle defining the occupied orbital [7]. To verify if this is the case we perform two-site cluster DFT+DMFT calculations, allowing for inequivalent neighboring Cr sites, i.e., for the lower symmetry of the monoclinic phase. More specifically, we use the cellular cluster DMFT approach and a $N \times N$ self-energy matrix per spin, where $N = N_o \times N_s$, and $N_o = 2$ is the number of orbitals per site and $N_s = 2$ the number of cluster sites. Surprisingly, we find that the orbital-order transition occurs at $T_{\rm KK}^{\rm M_T} \sim 400$ K, i.e., at temperatures very similar to the critical temperature $T_{\rm KK}^{\rm T}$. Furthermore, we find that down to 200 K the two sites have occupied orbitals defined by the angles $\theta = -\theta_1 \sim \theta_2 \sim 90^\circ$. Remarkably, there is no actual big difference between the sites, suggesting that super-exchange alone cannot account for the two inequivalent sites in this material. We also find a homogeneous solution in the presence of a tetragonal or a full (tetragonal and Jahn-Teller) crystal field.

Finally, we perform the same cluster DMFT calculations starting directly from the monoclinic structure (M in Fig. 3), again in the absence of the static crystal field. Because the hopping integrals decrease when the structure becomes monoclinic (Table I), super-exchange could become accordingly less strong; the presence of monoclinic distortions lowers, however, the symmetry of the super-exchange interaction and this could conversely by itself strongly enhance the tendency to orbital order. Surprisingly, we find that this is not the case. The transition temperature $T_{\rm KK}^{\rm M}$ remains about the same as $T_{\rm KK}^{\rm M_T}$, perhaps slightly smaller. We do find a slight site dependence of the occupied orbital, with $\theta_1 \sim -69^\circ$ and $\theta_2 \sim 123^\circ$ at $\sim$190 K. Although apparently this goes in the correct direction, i.e., towards the formation of inequivalent sites, the static crystal field associated with the monoclinic distortions has to be taken into account explicitly to explain the actual experimental difference in the occupied orbital for sites of type 1 and 2. The actual difference between $|\theta_1|$ and $|\theta_2|$ is explained by the larger tetragonal crystal-field splitting at sites of type 1 rather than by super-exchange.

C. Volume effect

A very different mechanism to which tilting and rotations in perovskites can be ascribed is the volume reduction with decreasing temperature; perhaps the tetragonal to monoclinic transition and the associated changes in the co-operative Jahn-Teller distortion can be explained by this phenomenon alone, without invoking strong correlation effects. Cation covalency can further help the stabilization of lower symmetry structures [21]. To clarify whether the 250-K transition is volume and covalency driven we compare the total energy of the different structures as a function of the volume. Since we have shown that the purely electronic super-exchange effect is not crucial, and since the volume effect is rather related to Slater exchange, we use for this purpose the GGA + U approach, sizably less expensive than DFT+DMFT but as well suited for this particular question. In Fig. 4 we show the total-energy curves obtained in GGA and SGGA. The GGA solutions are metallic. Having the largest hopping matrix elements of the three structures, the cubic structure is lowest in energy. The equilibrium volume is quite small as bringing the atoms closer together increases the hopping. Allowing for spin polarization the situation changes drastically. Exchange effects open a gap and lower all energy curves by about $\sim$2 eV. More importantly,

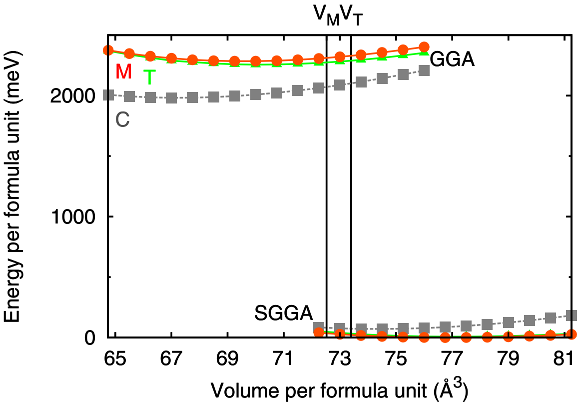

FIG. 4. (Color online) Energy vs volume calculated in the generalized-gradient approximation (GGA) and the spin-polarized generalized gradient approximation (SGGA). The experimental volumes in the tetragonal and monoclinic case are labeled as V$_T$ and V$_M$. Circles: monoclinic structure. Triangles: tetragonal. Squares: cubic. The lowest energy point is taken as the energy zero.

in SGGA the cubic structure is now energetically above the other structures. In the absence of a crystal-field splitting the orbital polarization, and hence the gain in exchange energy, is smaller than in the low-symmetry phases. To confirm this effect, we study the different structures in GGA + U, changing the volume by uniformly scaling the unit cell. As shown in Fig. 5, with increasing U the cubic structure becomes less and less favorable, as the orbital polarization of the insulating solution increases. We also observe that the position of the minimum in the energy curves shifts with increasing U to larger volumes. The reason is that for larger U the d-electrons tend to spread out to reduce their Hubbard energy. Thus the effective radius of the Cr ion, and therefore also the Cr-F equilibrium distance, increases with U. On the other hand, the effective K and F ionic radii, not involving any d electrons, do not change much. Consequently, with increasing U the tolerance factor decreases, favoring the tilting of the octahedra; i.e., with increasing U the monoclinic structure becomes more and more favorable. Overall, for a given volume, the tetragonal and monoclinic structures are very close in energy; in GGA the difference in energy $\Delta E_V = E_{\mathrm{M}}(V) - E_{\mathrm{T}}(V)$ is positive and ~30–40 meV for volumes V in the region between the GGA minima and the experimental volumes; ΔE_V becomes even smaller in GGA + U.

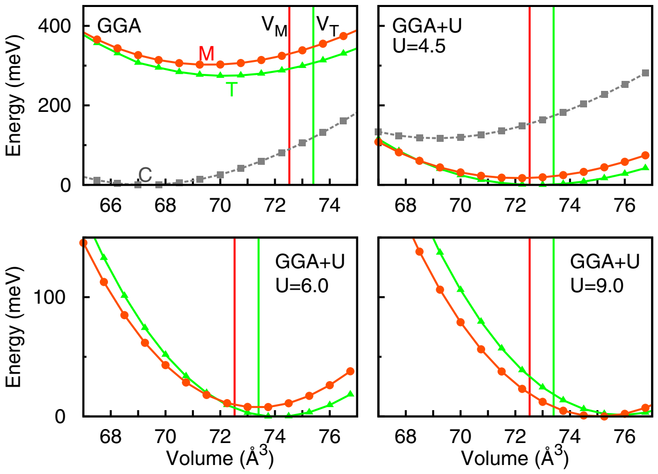

FIG. 5. (Color online) Energy per formula unit vs volume from GGA + U for increasing U. The energy zero corresponds in each case to the lowest energy point. The labels V$_T$ and V$_M$ indicate the experimental volume in the tetragonal and monoclinic structure. Circles: monoclinic structure. Triangles: tetragonal. Squares: cubic. At $U \sim 9$ eV the monoclinic structure becomes the lowest in energy. The volume is changed by uniformly scaling the unit cells.

Let us compare this to the super-exchange energy gain associated with orbital order, $-\Delta E_{\mathrm{KK}} \sim k_B T_{\mathrm{KK}}/2 \sim 20$ meV, with the energy differences between the various structures shown in Fig. 5 calculated in GGA. First we consider the energy difference between the tetragonal/monoclinic structures on the one hand and the cubic structure on the other; $|\Delta E_{\mathrm{KK}}|$ is an order of magnitude smaller than this energy difference, which is about (in absolute value) 200–300 meV. Thus $|\Delta E_{\mathrm{KK}}|$ alone cannot stabilize the tetragonal/monoclinic with respect to the cubic structure. This energy gain is rather associated with the static crystal-field splitting, which is ~840 meV in the tetragonal case, and the associated gain in exchange energy from orbital polarization. Next, we consider the GGA energy difference between the monoclinic and the tetragonal structure, ΔE_V. We have to compare it with the difference in orbital-order energy gain of the monoclinic structure with respect to the tetragonal structure, $\delta\Delta E_{\mathrm{KK}}$. Our results show that $|\delta\Delta E_{\mathrm{KK}}|$ is sizably smaller than $|\Delta E_V|$; it even has the wrong sign, i.e., $\delta\Delta E_{\mathrm{KK}}$ is positive rather than negative because $T_{\mathrm{KK}}^{\mathrm{M}}$ is slightly smaller than $T_{\mathrm{KK}}^{\mathrm{T}}$, and therefore would rather stabilize the tetragonal than the monoclinic structure. Thus Fig. 5 makes clear that it is rather the degree of localization and the corresponding change in the equilibrium Cr-F distance which controls the relative stability of the monoclinic and tetragonal structures.

If we also allow for spin-polarization, we obtain the SGGA + U results shown in Fig. 6. Other than in the preceding calculations we no longer rescale the unit cell, but optimize all cell parameters that, given the space group, can be varied. Consequently, we now find that the structure with the higher symmetry is always above the structure with a lower symmetry. All spin-polarized calculations yield an insulating ground state for all considered volumes. For the same reasons as discussed above, with increasing U the relative energy of the cubic structure increases as does the volume at which

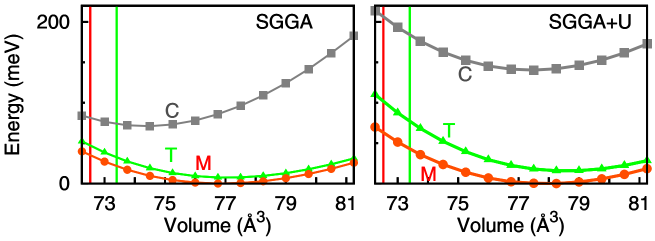

FIG. 6. (Color online) Energy per formula unit vs volume from SGGA + U calculations. The ground state is shifted at zero energy. The SGGA + U calculations are for $U = 6$ eV. Circles: monoclinic structure. Triangles: tetragonal. Squares: cubic. The vertical lines indicate the experimental volumes. For each structure all structural parameters are optimized.

the total-energy curves have their minimum. Since tilting the octahedra reduces the energy for small volumes, the monoclinic structure has its minimum at smaller volumes than the tetragonal. The energy (and structural) difference between the two becomes negligible for increasing volumes. This is in line with the observed structural transition. SGGA without U fails to reproduce the experimental c/a ratio in the monoclinic phase, but the agreement is recovered in SGGA + U calculations with realistic $U \sim 5$–6 eV. Remarkably, the energy gain from lowering the symmetry from tetragonal to monoclinic, ΔE_V, is tiny, $\sim\!-10$ meV in SGGA and $\sim\!-15$ meV in SGGA + U with $U \sim 6$ eV. This is in line with a tetragonal to monoclinic transition at temperatures as low as 250 K.

As we have seen, orbital many-body super-exchange appears to hardly affect this energy balance. Even a difference in energy as small as 10 meV would correspond to a temperature difference $T_{\rm KK}^{\rm T} - T_{\rm KK}^{\rm M} \sim 2\delta\Delta_{\rm KK}/k_B$ of the order of 200 K, whereas our results indicate that the super-exchange transition temperature is about the same in the monoclinic and tetragonal phase, and has furthermore the incorrect sign ($\delta\Delta_{\rm KK} > 0$). The difference $|\delta\Delta_{\rm KK}|$ could increase if the screened Coulomb repulsion integral U would be very different for the monoclinic and tetragonal structure. Even if the Coulomb repulsion is slightly different in the two phases, however, it is unlikely that it is reduced by 50% in the monoclinic phase, as would be required to explain a monoclinic ground state within super-exchange. Furthermore our *ab-initio* estimates of U indicates that this parameter is slightly larger in the monoclinic than in the tetragonal phase; such a difference would lead again to a positive rather than negative $\delta\Delta_{\rm KK}$, reinforcing the conclusion that super-exchange alone does not explain the tetragonal to monoclinic transition.

On the other hand, in the presence of static distortions a redistribution of orbital occupations follows, and it is strongly enhanced by the Coulomb repulsion; this can further stabilize the low-symmetry structures with respect the cubic one. The e_g crystal-field splitting is modified from $\sim$840 meV in the tetragonal structure to $\sim$950 meV (site 1) and $\sim$680 meV (site 2). Our DMFT calculations show that, differently than in GGA, in the presence of such crystal-field splittings, the occupation at a temperature as high as 550 K is already basically complete for both the tetragonal and the monoclinic structure. Our cluster DMFT results indicate that there is no sizable charge disproportionation, despite the difference in crystal-field splitting between sites of types 1 and 2.

D. Magnetic superexchange

In this last section we analyze the magnetic structure. The aim is to verify if the change in orbital order resulting from our calculations for the experimental structure can explain the observed magnetic order in the monoclinic phase. To do this we calculate the magnetic coupling using super-exchange theory in the basis of Wannier functions [6,30] for the high-spin $t_{2g}^3 e_g^1$ electronic configuration. The magnetic coupling has contributions from both the half filled t_{2g} shell and the e_g shell; in a basis of orthogonal Wannier functions we can split the two contributions so that $J^{i,i'} = J^{i,i'}_{e_g} + J^{i,i'}_{t_{2g}}$. Then, if we neglect spin-flip and pair-hopping terms we arrive at the approximate expressions

$$J^{i,i'}_{e_g} \sim \frac{\left|t^{i,i'}_{a,a}\right|^2}{U + 3J + \varepsilon^i_a - \varepsilon^{i'}_a} + \frac{\left|t^{i,i'}_{a,a}\right|^2}{U + 3J + \varepsilon^{i'}_a - \varepsilon^i_a} - \frac{\left|t^{i,i'}_{a,b}\right|^2}{U - 3J + \varepsilon^{i'}_b - \varepsilon^i_a}\frac{4J}{U + J + \varepsilon^{i'}_b - \varepsilon^i_a} - \frac{\left|t^{i',i}_{a,b}\right|^2}{U - 3J + \varepsilon^i_b - \varepsilon^{i'}_a}\frac{4J}{U + J + \varepsilon^i_b - \varepsilon^{i'}_a},$$

$$J^{i,i'}_{t_{2g}} \sim 2\frac{\left|t^{i,i'}_{c,c}\right|^2 + \left|t^{i,i'}_{d,d}\right|^2 + \left|t^{i,i'}_{e,e}\right|^2}{U + 3J}.$$

Here we denote with $|a\rangle$ and $|b\rangle$ the e_g crystal-field states and with $|c\rangle$, $|d\rangle$, $|e\rangle$ the t_{2g} crystal-field states; we find that $|c\rangle \sim |xy\rangle$, $|d\rangle \sim |yz\rangle$, $|e\rangle \sim |xz\rangle$. The crystal-field splittings and the hoppings among the t_{2g} orbitals are given in Table II. Since for the t_{2g} states we find that the interorbital hopping integrals are very small, for simplicity we set them to zero in the formula above; for the same reason we set to zero the energy difference between crystal-field orbitals at different sites, which is at most 120 meV and leads to small corrections of order $(t^2/U)(\Delta\varepsilon/U)^2$. The calculated exchange couplings (including also the small contributions neglected in the analytic expression above) are shown in Fig. 7. This figure shows that if the tetragonal structure would persist at low temperature, the magnetic structure would be ferromagnetic and isotropic in the xy plane, and antiferromagnetic along the **z** axis. In the monoclinic structure the coupling in the xy plane remains ferromagnetic, with the ferromagnetic coupling slightly anisotropic, because the interorbital t_{2g} hoppings are small, hence the antiferromagnetic contribution dominates. Remarkably, ferromagnetism in the xy plane can then be ascribed to orbital order in the e_g states alone. On the other hand the t_{2g} states are essential for the antiferromagnetic order along **z**. All this is in excellent agreement with experiment. Thus the orbital order obtained in our calculation supports the experimentally reported magnetic

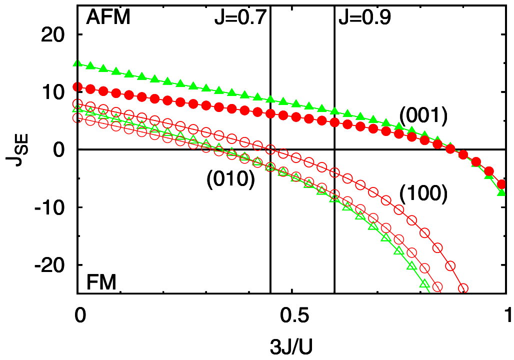

FIG. 7. (Color online) Super-exchange parameters as function of $3J/U$ for $U = 6$ eV. Triangles: tetragonal structure. Circles: monoclinic structure. Full symbols: coupling along the **z** axis. Empty symbols: coupling along **x** and **y**. The directions **x**, **y**, and **z** are defined in the caption of Table I. The two vertical lines indicate realistic values of the $3J/U$ ratio. In this range super-exchange yields an A-type antiferromagnetic structure, in agreement with experiments.

TABLE II. Largest nearest neighbor hopping integrals $t^{i,i'}_{m,m'}$ and crystal-field matrix elements $\varepsilon_{m,m'}$ in the t_{2g}-like basis, with $|1\rangle = |xy\rangle$, $|2\rangle = |yz\rangle$, and $|3\rangle = |xz\rangle$. All energies are in meV. For the crystal-field levels we take $\varepsilon_{1,1}$ at site 1 as energy zero. The directions $\mathbf{x} = (100)$, $\mathbf{y} = (010)$, and $\mathbf{z} = (001)$ are defined in the caption of Fig. 1.

	Cubic			Tetragonal			Monoclinic		
lmn	$t^{i,i'}_{1,1}$	$t^{i,i'}_{2,2}$	$t^{i,i'}_{3,3}$	$t^{i,i'}_{1,1}$	$t^{i,i'}_{2,2}$	$t^{i,i'}_{3,3}$	$t^{i,i'}_{1,1}$	$t^{i,i'}_{2,2}$	$t^{i,i'}_{3,3}$
100	−102	−3	−102	−94	−3	−89	−113	0	−132
010	−102	−102	−3	−94	−89	−3	−75	−88	0
001	−3	−102	−102	−6	−144	−144	−1	−91	−86
	$\varepsilon_{1,1}$	$\varepsilon_{2,2}$	$\varepsilon_{3,3}$	$\varepsilon_{1,1}$	$\varepsilon_{2,2}$	$\varepsilon_{3,3}$	$\varepsilon^{\mathrm{Cr1}}_{1,1}$	$\varepsilon^{\mathrm{Cr1}}_{2,2}$	$\varepsilon^{\mathrm{Cr1}}_{3,3}$
000	0	0	0	0	43	−86	0	−70	−96
							$\varepsilon^{\mathrm{Cr2}}_{1,1}$	$\varepsilon^{\mathrm{Cr2}}_{2,2}$	$\varepsilon^{\mathrm{Cr2}}_{3,3}$
							−123	−29	−3

structure. Finally, by comparing crystal-field energies with and without spin-orbit interaction, we obtain the spin-orbit couplings (Table I) and find them small in all systems, but larger in the monoclinic than in the tetragonal or cubic structures. Thus we additionally perform SGGA + U magnetocrystalline anisotropy calculations and find that a spin orientation in the **xy** plane is favored, in line with experiments [2]; our results suggest **y** as an easy axis, but the energy difference between **y** and **x** is tiny (0.03 meV).

IV. CONCLUSION

We have studied the origin of orbital order and structural phase transitions in KCrF$_3$, a system which is isoelectronic to LaMnO$_3$. We could reproduce the experimental orbital and spin order in all phases. We show that the Kugel-Khomskii super-exchange mechanism is not strong enough to drive the high-temperature cubic to tetragonal transition reported at 973 K. The tetragonal to monoclinic transition is more tricky, because the super-exchange transition temperature is larger than the structural transition temperature. By using the cluster DFT+DMFT approach we show, however, that super-exchange does not support the experimental type of orbital order in the monoclinic phase. Next we analyze the stability of the various phases as a function of volume. We show, by using GGA + U and SGGA + U, that the tetragonal phase is favored at larger volumes and the monoclinic at small volumes, in agreement with experiments. The difference in energy is small, ∼10–20 meV, again in agreement with experiments. The exact volume of the transition from tetragonal to monoclinic depends on U and the spin polarization. Increasing U the transition happens at larger and larger volumes. The change in structure is thus helped more by Slater exchange than by super-exchange; a triggering factor could be a slightly larger direct Coulomb repulsion integral U in the monoclinic structure. Once the distortions are in place, DMFT calculations show that the orbital polarization is enhanced by Coulomb repulsion, likely providing a positive feedback to the stabilization of the distorted structure.

ACKNOWLEDGMENTS

Calculations have been done on the Jülich Blue Gene/Q and Juropa. C.A. acknowledges financial support from the Fondazione Angelo Della Riccia and discussions with M. Cuoco. E.P. and E.K. acknowledge financial support from the Deutsche Forschungsgemeinschaft through research unit FOR 1346.

---

[1] S. Margadonna and G. Karotsis, J. Am. Chem. Soc. **128**, 16436 (2006); J. Mater. Chem. **17**, 2013 (2007).

[2] Y. Xiao, Y. Su, H.-F. Li, C. M. N. Kumar, R. Mittal, J. Persson, A. Senyshyn, K. Gross, and Th. Brueckel, Phys. Rev. B **82**, 094437 (2010).

[3] G. Giovannetti, S. Margadonna, and J. van den Brink, Phys. Rev. B **77**, 075113 (2008).

[4] L. G. Marshall, J. Zhou, J. Zhang, J. Han, S. C. Vogel, Y. Zhao, M. T. Fernández-Díaz, X. Yu, J. Cheng, and J. B. Goodenough, Phys. Rev. B **87**, 014109 (2013).

[5] Y. Xu, X. Hao, M. Lv, Z. Wu, D. Zhou, and J. Meng, J. Chem. Phys. **128**, 164721 (2008).

[6] E. Pavarini, E. Koch, and A. I. Lichtenstein, Phys. Rev. Lett. **101**, 266405 (2008).

[7] E. Pavarini and E. Koch, Phys. Rev. Lett. **104**, 086402 (2010).

[8] A. Flesch, G. Zhang, E. Koch, and E. Pavarini, Phys. Rev. B **85**, 035124 (2012).

[9] K. I. Kugel and D. I. Khomskii, Zh. Eksp. Teor. Fiz. **64**, 1429 (1973) [Sov. Phys. JETP **37**, 725 (1973)].

[10] J. Rodríguez-Carvajal, M. Hennion, F. Moussa, A. H. Moudden, L. Pinsard, and A. Revcolevschi, Phys. Rev. B **57**, R3189 (1998); J.-S. Zhou and J. B. Goodenough, *ibid.* **68**, 144406 (2003); Phys. Rev. Lett. **96**, 247202 (2006).

[11] Using the local-density approximation (LDA) instead of the GGA does not alter our conclusions.

[12] V. I. Anisimov, A. I. Poteryaev, M. A. Korotin, A. O. Anokhin, and G. Kotliar, J. Phys.: Condens. Matter **9**, 7359 (1997); A. I. Lichtenstein and M. I. Katsnelson, Phys. Rev. B **57**, 6884 (1998).

[13] *The LDA+DMFT Approach to Strongly Correlated Materials*, edited by E. Pavarini, E. Koch, D. Vollhardt, and A. Lichtenstein, Modeling and Simulation Vol. 1 (Verlag des Forschungszentrum, Jülich, 2011).

[14] V. I. Anisimov, J. Zaanen, and O. K. Andersen, Phys. Rev. B **44**, 943 (1991).

[15] V. I. Anisimov, I. V. Solovyev, M. A. Korotin, M. T. Czyzyk, and G. A. Sawatzky, Phys. Rev. B **48**, 16929 (1993).

[16] A. I. Liechtenstein, V. I. Anisimov, and J. Zaanen, Phys. Rev. B **52**, R5467 (1995).

[17] M. Torrent, F. Jollet, F. Bottin, G. Zerah, and X. Gonze, Comput. Mater. Sci. **42**, 337 (2008).

[18] X. Gonze *et al.*, Comput. Phys. Commun. **180**, 2582 (2009).

[19] G. Kresse and D. Joubert, Phys. Rev. B **59**, 1758 (1999).

[20] A. A. Mostofi, J. R. Yates, Y. S. Lee, I. Souza, D. Vanderbilt, and N. Marzari, Comput. Phys. Commun. **178**, 685 (2008).

[21] E. Pavarini, A. Yamasaki, J. Nuss, and O. K. Andersen, New J. Phys. **7**, 188 (2005).

[22] K. H. Ahn and A. J. Millis, Phys. Rev. B **61**, 13545 (2000).

[23] G. Zhang, E. Gorelov, E. Koch, and E. Pavarini, Phys. Rev. B **86**, 184413 (2012).

[24] M. Cococcioni and S. de Gironcoli, Phys. Rev. B **71**, 035105 (2005).

[25] T. Mizokawa and A. Fujimori, Phys. Rev. B **54**, 5368 (1996).

[26] J. E. Hirsch and R. M. Fye, Phys. Rev. Lett. **56**, 2521 (1986).

[27] E. Gull, A. J. Millis, A. I. Lichtenstein. A. N. Rubtsov, M. Troyer, and P. Werner, Rev. Mod. Phys. **83**, 349 (2011).

[28] A. Flesch, E. Gorelov, E. Koch, and E. Pavarini, Phys. Rev. B **87**, 195141 (2013).

[29] A. Yamasaki, M. Feldbacher, Y.-F. Yang, O. K. Andersen, and K. Held, Phys. Rev. Lett. **96**, 166401 (2006).

[30] E. Pavarini, S. C. Tarantino, T. B. Ballaran, M. Zema, P. Ghigna, and P. Carretta, Phys. Rev. B **77**, 014425 (2008).